

Propulsion of bullet- and cup-shaped nano- and microparticles by traveling ultrasound waves

Johannes Voß¹ and Raphael Wittkowski^{1,*}

¹*Institut für Theoretische Physik, Center for Soft Nanoscience,
Westfälische Wilhelms-Universität Münster, 48149 Münster, Germany*

The propulsion of colloidal particles via planar traveling ultrasound waves has attracted increasing attention in recent years. A frequently studied type of particles is bullet-shaped and cup-shaped nano- and microparticles. Based on acoustofluidic simulations, this article investigates how the propulsion of bullet-shaped particles depends on their length and diameter, where cup-shaped particles are included as limiting cases corresponding to the smallest particle length. The structure of the flow field generated by the particles is discussed and it is shown that the particles' propulsion strength increases with their length and diameter. When varying the diameter, we observed also a sign change of the propulsion. This work complements previous experimental studies that have addressed such particles only for particular aspect ratios, and the provided understanding of how the propulsion of the particles depends on their dimensions will prospectively be helpful for the choice of particle shapes that are most suitable for future experimental studies.

I. INTRODUCTION

Since their discovery in 2012 [1], ultrasound-propelled nano- and microparticles are a rapidly growing target for research [1–55]. The research on this type of artificial motile particles is driven by the prospect of applying these particles in the future as useful nano- or microdevices that can perform medical tasks [56–62] or form active materials with intriguing properties [63–65]. So far, research on ultrasound-propelled nano- and microparticles has mainly been experimental [1–3, 5–14, 18–25, 27, 28, 30–35, 37–40, 42, 43, 45, 46, 66, 67], but there have also been some publications that are based on acoustofluidic simulations [21, 31–34, 37, 40, 44, 49, 52–55] and two studies that rely on analytical approaches [4, 26].

Despite the intensive research on acoustically propelled particles, the understanding of these particles is still very limited. For example, little is known about how the propulsion of the particles depends on their shape. A reason for this limited knowledge is the fact that research on these particles is mainly experimental and it is much more difficult to vary the particle shape in experiments than in theory. Up to now, mostly bullet-shaped particles have been studied [1–4, 6–9, 12, 13, 16, 18, 20, 22, 23, 26–28, 30, 33–35, 38, 46, 48, 68, 69]. These are rod-shaped particles with a concave end and a convex end. Some studies have addressed hemi-spherical cups (nanoshells) [19, 37, 44], which can be interpreted as the limit of a bullet-shaped particle with hemi-spherical ends for decreasing length of the cylindrical part between the two ends. There are also studies on cone-shaped particles [44, 49, 52–54], a gear-shaped particle [21, 25, 31], and microspinnners [55].

Although bullet-shaped particles are frequently used, only particles with a few particular diameters and lengths

have been realized [1–4, 6–9, 12, 13, 16, 18, 20, 22, 23, 26–28, 30, 33–35, 38, 46, 48, 68, 69]. Furthermore, the shape of the ends of the particles used in experiments was either hemi-spherical [2, 3, 6–8, 12, 13, 16, 18, 20, 23, 28, 30, 35, 38] or irregular due to a less-controlled fabrication process [1–3, 6–9, 12, 13, 16, 18, 22, 23, 27, 28, 30, 33, 35, 38, 46, 48, 68, 69]. In the analytical study [26], bullet-shaped particles with hemi-spherical and hemi-spheroidal ends were studied, where the concavity and convexity of the ends were varied. This study found that the propulsion velocity depends strongly on the concavity and convexity of the ends. When varying the shape of the ends, even a change in the propulsion direction of the particle was observed. For the hemi-spherical-cup particles [19, 37, 44], the opposite propulsion direction as for bullet-shaped particles with hemi-spherical ends was found. A problem additional to this limited insight into the shape-dependence of the acoustic propulsion is the fact that all except for a few [32, 49, 52–55] previous studies addressed particles in a standing ultrasound wave, whereas traveling ultrasound waves are much more relevant for the envisaged future applications of acoustically propelled particles [44, 49, 52].

In this article, we aim at extending the understanding of the effect the particle shape has on the particles' propulsion. We focus on bullet-shaped nano- and microparticles with hemi-spherical ends, as they have been applied in previous experiments [2, 3, 6–8, 12, 13, 16, 18, 20, 23, 28, 30, 35, 38], and study, based on direct acoustofluidic simulations, how the flow field generated by the particles and the strength of their propulsion depend on the length and diameter of the particles. By including the limit of very short particles, where the concave and convex hemi-spherical ends get very close, we cover also hemi-spherical-cup particles. This allows us to understand at which particle length the sign change of the propulsion velocity, which is indicated by the previous experimental work, occurs. Different from most previous studies, we consider a traveling

* Corresponding author: raphael.wittkowski@uni-muenster.de

instead of a standing ultrasound wave to get more insight into this particularly application-relevant case.

II. METHODS

For consistency and to rely on methods that have been proven to be successful, our methodology is adopted from Ref. [44].

A. Setup

An overview of the simulated system is given in Fig. 1. The system includes a rectangular fluid-filled domain and

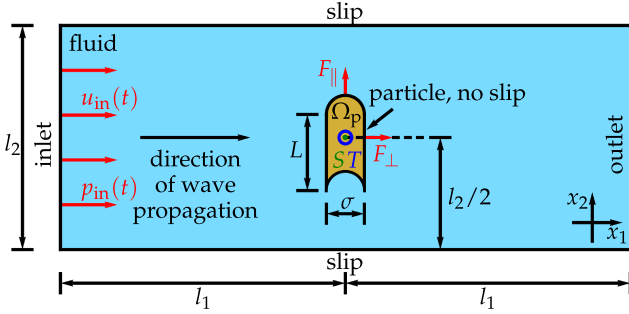


FIG. 1. Setup for the simulations.

a bullet-shaped particle in the center of the domain. We place the particle such that its center of mass S coincides with the geometric center of the rectangular domain. The particle's shape is fixed, i.e., we consider a solid particle. It consists of a cylindrical part and two hemi-spherical ends of which one is concave and one is convex. This shape is motivated by previous experimental studies [1–3, 6, 8, 9, 12, 19, 20, 27, 28, 33, 34, 37, 44, 46]. We orientate the particle in such a way that the vector from the center of the lower end of the particle to the center of its upper end points in the x_2 -direction. The rectangular domain has width $2l_1$ (oriented parallel to the x_1 -axis) and height $l_2 = 200 \mu\text{m}$ (oriented parallel to the x_2 -axis) and the particle has variable diameter $\sigma \in [0.5, 5] \mu\text{m}$ and a cylindrical part of variable length $L \in [0.1, 5] \mu\text{m}$.

Because of its general relevance, we choose water as the fluid. When the simulation starts at time $t = 0$, the water shall have a vanishing velocity field $\vec{u}_0 = \vec{0} \text{ m s}^{-1}$. Moreover, the water shall initially be at standard temperature $T_0 = 293.15 \text{ K}$ and standard pressure $p_0 = 101325 \text{ Pa}$, where it has mass density $\rho_0 = 998 \text{ kg m}^{-3}$, shear viscosity $\nu_s = 1.002 \text{ mPa s}$, bulk viscosity $\nu_b = 2.87 \text{ mPa s}$, and sound velocity $c_f = 1484 \text{ m s}^{-1}$.

A planar traveling ultrasound wave enters the system at its left edge (inlet), propagates in the x_1 -direction, interacts with the particle, and can leave the system at its right edge (outlet). At the inlet, we, therefore, prescribe a time-dependent velocity $u_{\text{in}}(t) = \Delta u \sin(2\pi f t)$ and pressure $p_{\text{in}}(t) = \Delta p \sin(2\pi f t)$, where $\Delta u = \Delta p / (\rho_0 c_f)$ is

the velocity amplitude of the entering ultrasound wave, $\Delta p = 10 \text{ kPa}$ its pressure amplitude, and $f = 1 \text{ MHz}$ its frequency. For the lower and upper edges of the simulation domain, we choose slip boundary conditions, and we use no-slip boundary conditions at the boundary of the particle domain Ω_p . Our choice for the pressure amplitude Δp corresponds to an acoustic energy density $E = \Delta p^2 / (2\rho_0 c_f^2) = 22.7 \text{ mJ m}^{-3}$ that is considered to be harmless for humans and thus suitable for diagnostic applications [70]. The choice for the frequency f is slightly lower than the frequencies that are common in sonography. For the wavelength of the ultrasound, we obtain $\lambda = c_f / f = 1484 \text{ mm}$. As in Refs. [44, 49, 52, 54, 55], we choose the width of the simulation domain so that $l_1 = \lambda / 4$.

The interaction of the ultrasound with the particle causes forces and torques acting on the particle. We are interested in the stationary time-averaged propulsion force F_{\parallel} that is oriented parallel to the particle, the stationary time-averaged propulsion force F_{\perp} that is oriented perpendicular to the particle, and the stationary time-averaged propulsion torque T that tends to rotate the particle in the x_1 - x_2 -plane. Both force components and the torque act on the center of mass S and are measured in the laboratory frame.

B. Parameters

Table I shows the names and symbols of the parameters that are relevant for our simulations and their values that we have chosen in analogy to the values used in Ref. [44].

C. Acoustofluidic simulations

We use direct computational fluid dynamics simulations to simulate the propagation of the ultrasound and its interaction with the particle. They consist of solving the standard equations of fluid dynamics (continuity equation, compressible Navier-Stokes equations, linear constitutive equation for the pressure).

The dimensionless numbers that result from these equations by nondimensionalization are the Euler number

$$\text{Eu} = \frac{\Delta p}{\rho_0 \Delta u^2} \approx 2.2 \cdot 10^5, \quad (1)$$

Helmholtz number

$$\text{He} = \frac{f \max\{L, \sigma\}}{c_f} \approx 3.37 \cdot 10^{-4} - 3.37 \cdot 10^{-3}, \quad (2)$$

bulk Reynolds number

$$\text{Re}_b = \frac{\rho_0 \Delta u \max\{L, \sigma\}}{\nu_b} \approx 1.17 \cdot 10^{-3} - 1.17 \cdot 10^{-2}, \quad (3)$$

TABLE I. Relevant parameters and the corresponding values. For consistency, the values are chosen analogously to Ref. [44].

Name	Symbol	Value	Remark
Particle diameter	σ	0.5-5 μm	
Particle length	L	0.1-5 μm	
Sound frequency	f	1 MHz	
Speed of sound	c_f	1484 m s^{-1}	Corresponds to T_0 and p_0
Time period of sound	$\tau = 1/f$	1 μs	
Wavelength of sound	$\lambda = c_f/f$	1.484 mm	
Temperature of fluid	T_0	293.15 K	
Mean mass density of fluid	ρ_0	998 kg m^{-3}	Corresponds to T_0 and p_0
Mean pressure of fluid	p_0	101 325 Pa	
Initial velocity of fluid	\vec{u}_0	$\vec{0} \text{ m s}^{-1}$	
Sound pressure amplitude	Δp	10 kPa	
Flow velocity amplitude	$\Delta u = \Delta p/(\rho_0 c_f)$	6.75 mm s^{-1}	
Acoustic energy density	$E = \Delta p^2/(2\rho_0 c_f^2)$	22.7 mJ m^{-3}	
Shear/dynamic viscosity of fluid	ν_s	1.002 mPa s	Corresponds to T_0 and p_0
Bulk/volume viscosity of fluid	ν_b	2.87 mPa s	Interpolated from Tab. 1 in Ref. [71] for T_0 and p_0
Inlet-particle distance	l_1	$\lambda/4$	
Domain width	l_2	200 μm	
Mesh-cell size	Δx	15 nm-1 μm	
Time-step size	Δt	1-10 ps	
Simulation duration	t_{max}	$\geq 500\tau$	
Euler number	Eu	$2.2 \cdot 10^5$	
Helmholtz number	He	$3.37 \cdot 10^{-4}$ - $3.37 \cdot 10^{-3}$	
Bulk Reynolds number	Re _b	$1.17 \cdot 10^{-3}$ - $1.17 \cdot 10^{-2}$	
Shear Reynolds number	Re _s	$3.36 \cdot 10^{-3}$ - $3.36 \cdot 10^{-2}$	
Particle Reynolds number	Re _p	$< 2 \cdot 10^{-6}$	

and shear Reynolds number

$$\text{Re}_s = \frac{\rho_0 \Delta u \max\{L, \sigma\}}{\nu_s} \approx 3.36 \cdot 10^{-3} - 3.36 \cdot 10^{-2}. \quad (4)$$

Considering the motion of the particle in the fluid that can result from the propulsion force and torque acting on the particle, one can also define a particle Reynolds number

$$\text{Re}_p = \frac{\rho_0}{\nu_s} \max\{L, \sigma\} \sqrt{v_{\parallel}^2 + v_{\perp}^2} < 2 \cdot 10^{-6}, \quad (5)$$

where v_{\parallel} and v_{\perp} are the propulsion velocities that correspond to F_{\parallel} and F_{\perp} , respectively (see Section II E). See Ref. [49] for an interpretation of these dimensionless numbers.

We solve the equations of fluid dynamics with the finite volume software package OpenFOAM [72]. For spatial discretization of the studied system, we use a structured, mixed rectangular-triangular mesh with about 300,000 cells. The cell size Δx is very small close to the particle and increases with the distance from the particle. For temporal discretization of the time range from $t = 0$, where a simulation starts, to $t = t_{\text{max}} \geq 500\tau$ with the period $\tau = 1/f$ of the ultrasound wave, where the simulation ends, we use an adaptive time-step method. The time-step size Δt always has to fulfill the Courant-Friedrichs-Lewy condition

$$C = c_f \frac{\Delta t}{\Delta x} < 1. \quad (6)$$

Since these simulations require a fine discretization in space and time, the typical computational expense of an individual simulation run amounts to 36,000 CPU core hours.

D. Propulsion force and torque

From the results of the acoustofluidic simulations, we obtain the stationary time-averaged propulsion force components F_{\parallel} and F_{\perp} and propulsion torque T by suitable integration of the stress tensor Σ over the particle surface, locally averaging over one period, and extrapolating towards $t \rightarrow \infty$ (see Ref. [44] for details on this procedure). By distinguishing the pressure component $\Sigma^{(p)}$ and the viscous component $\Sigma^{(v)}$ of the stress tensor $\Sigma = \Sigma^{(p)} + \Sigma^{(v)}$, we can split F_{\parallel} , F_{\perp} , and T as $F_{\parallel} = F_{\parallel,p} + F_{\parallel,v}$, $F_{\perp} = F_{\perp,p} + F_{\perp,v}$, and $T = T_p + T_v$ into a pressure contribution (subscript “p”) that originates from $\Sigma^{(p)}$ and a viscous contribution (subscript “v”) that originates from $\Sigma^{(v)}$.

E. Translational and angular propulsion velocity

Using the Stokes law [73], we calculate from F_{\parallel} , F_{\perp} , and T the corresponding translational propulsion velocity parallel to the particle’s orientation v_{\parallel} , translational propulsion velocity perpendicular to the particle’s ori-

entation v_{\perp} , and angular propulsion velocity ω . This transformation (see Ref. [44] for details) involves the hydrodynamic resistance matrix \mathbf{H} , which depends on the size and shape of the particle. For better reproducibility of our results, we here present the hydrodynamic resistance matrix for the particle studied in the present work, which can be calculated, e.g., with the software `HydResMat` [74, 75]. When choosing the center of mass S as the reference point for the calculation of \mathbf{H} and assigning a thickness of σ in the third dimension to the particle (see Ref. [44] for details), \mathbf{H} has the general structure

$$\mathbf{H} = \begin{pmatrix} K_{11} & 0 & 0 & 0 & 0 & C_{31} \\ 0 & K_{22} & 0 & 0 & 0 & 0 \\ 0 & 0 & K_{33} & C_{13} & 0 & 0 \\ 0 & 0 & C_{13} & \Omega_{11} & 0 & 0 \\ 0 & 0 & 0 & 0 & \Omega_{22} & 0 \\ C_{31} & 0 & 0 & 0 & 0 & \Omega_{33} \end{pmatrix}. \quad (7)$$

The values of the nonzero elements are given in Tab. II for each particle diameter σ and length L considered in this work.

III. RESULTS AND DISCUSSION

In this section, we present our simulation results for the time-averaged stationary flow field that forms around a bullet-shaped particle as depicted in Fig. 1 and for the strength of the associated time-averaged stationary propulsion of the particle. We varied the length $L \in [0.1, 5] \mu\text{m}$ of the particle while keeping its diameter constant at $\sigma = 0.5 \mu\text{m}$, and we varied the particle's diameter $\sigma \in [0.5, 5] \mu\text{m}$ while keeping its length constant at $L = 0.1 \mu\text{m}$, to study the influence of these parameters on the flow field and propulsion strength. In the first case, the particle is an increasingly elongated bullet, whereas in the second case, it is a hemi-spherical cup with increasing size.

A. Flow field

Our simulation results for the time-averaged stationary flow field that forms around the particle are shown in Fig. 2.

For our discussion of the flow field, we consider a cup-shaped particle with diameter $\sigma = 0.5 \mu\text{m}$ and length $L = 0.1 \mu\text{m}$ (see Fig. 2a) as a reference particle. We can see that the flow field around this particle is dominated by four large vortices, whose centers are located at the top left, top right, bottom left, and bottom right of the particle. Their distances from the center of mass of the particle are similar. In addition, there are two small and weak vortices near the concave end of the particle. The rotation directions of the large vortices are such that the fluid flows laterally towards the particle and above and below the particle away from it. As a consequence,

the pressure is laterally increased and above and below the particle decreased. Flow fields with a qualitatively similar structure (but for convex particle shapes without the small vortices) have already been observed for solid or hollowed-out half-sphere-shaped particles [44] and for solid [49, 52–54] or hollowed-out [44] cone-shaped or triangular particles. In the present case, the centers of the large vortices above the particle are slightly nearer to the particle's center of mass than those below the particle.

1. Variation of length L

First, we discuss the dependence of the particle's flow field on the particle's length L . When, starting at the reference particle, we increase L from $L = 0.1 \mu\text{m}$ to $L = 1 \mu\text{m}$, the centers of the large vortices move slowly away from the center of mass of the particle, while the distances of the centers of the large vortices from the center of mass of the particle remain similar. However, if we increase the length to $L = 5 \mu\text{m}$, we obtain a qualitatively different flow field, which is less symmetric. While the centers of the four large vortices move further away from the center of mass of the particle, the two right vortex centers now move away much faster than the two left ones (in Fig. 2d, the large right vortices are therefore outside of the plotted region). The distances of the centers of the large vortices from the center of mass of the particle are $\approx 11.6 \mu\text{m}$ for the left vortices and $\approx 33.2 \mu\text{m}$ for the right ones. This leads to an asymmetric arrangement of the vortices. Furthermore, two additional smaller vortices close to the particle occur now at its bottom left and bottom right. The distance of the two smaller vortices from the center of mass of the particle is $\approx 4.1 \mu\text{m}$. We can also see that, when increasing L from $L = 0.1 \mu\text{m}$ to $L = 5 \mu\text{m}$, the flow near the particle becomes faster.

2. Variation of diameter σ

Next, we discuss how the particle's flow field depends on the particle's diameter σ . When we increase σ from $\sigma = 0.5 \mu\text{m}$ to $\sigma = 1 \mu\text{m}$, the centers of the large vortices again move slowly away from the center of mass of the particle. However, now the distance of the two lower vortex centers from the center of mass of the particle increases significantly faster than the distance of the two upper vortex centers. Increasing the diameter further to $\sigma = 2 \mu\text{m}$ leads to a qualitatively different flow field. Now, the two large vortices below the particle vanish and the two small vortices inside the cavity of the particle increase and move further below the particle. Far below the particle, the fluid flows still away from the particle, but close to the particle the lower two vortices now lead to a flow that runs parallel to the symmetry axis of the particle towards the center of the particle, from there along the lower particle surface to the edge of the particle, then around the vortices below the particle, and

TABLE II. Nonzero elements of the hydrodynamic resistance matrix \mathbf{H} of the particle that is considered in this article (see Fig. 1).

$\sigma/\mu\text{m}$	$L/\mu\text{m}$	$\mathbf{K}_{11}/\mu\text{m}$	$\mathbf{K}_{22}/\mu\text{m}$	$\mathbf{K}_{33}/\mu\text{m}$	$\mathbf{C}_{13}/\mu\text{m}^2$	$\mathbf{C}_{31}/\mu\text{m}^2$	$\mathbf{\Omega}_{11}/\mu\text{m}^3$	$\mathbf{\Omega}_{22}/\mu\text{m}^3$	$\mathbf{\Omega}_{33}/\mu\text{m}^3$
0.5	5	21.91	15.36	21.68	-0.73	1.74	86.08	6.48	89.32
0.5	1	9.08	7.68	8.81	-0.42	0.84	3.17	1.74	3.54
0.5	0.5	6.96	6.41	6.65	-0.31	0.66	1.23	1.13	1.42
0.5	0.1	4.95	5.12	4.50	-0.20	0.51	0.44	0.61	0.53
1	0.1	9.39	9.96	8.41	-0.76	2.01	3.09	4.35	3.72
2	0.1	17.92	19.16	15.82	-2.58	7.68	22.37	31.81	27.03
5	0.1	43.79	47.42	38.56	-15.29	47.95	333.19	472.74	405.73

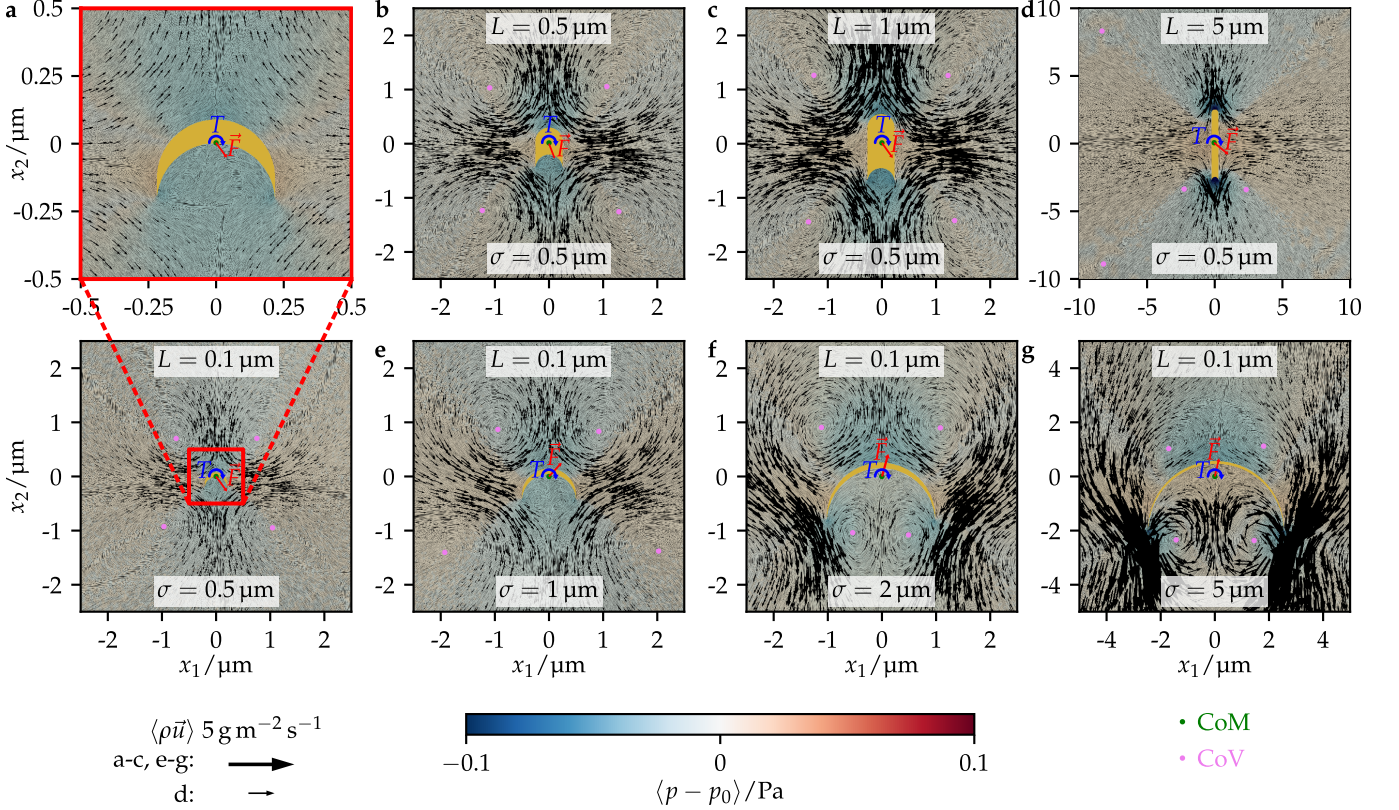


FIG. 2. Time-averaged stationary mass-current density $\langle \rho \vec{u} \rangle$ and reduced pressure $\langle p - p_0 \rangle$ around bullet- and cup-shaped acoustically propelled particles (see Fig. 1) with different diameters σ and lengths L . The particle's center of mass (CoM), the fluid's centers of vortices (CoV), and the orientations of the propulsion force \vec{F} and torque \vec{T} that are exerted on the particle are indicated.

again towards the center of the particle. The distances of the centers of the four vortices from the center of mass of the particle are similar, but the vortex centers below the particle are nearer to each other than the upper vortex centers are. Further increasing the diameter to $\sigma = 5 \mu\text{m}$ leads to larger distances of all vortex centers from the center of mass of the particle, where the vortex centers below the particle increase their distance from the center of mass of the particle faster than the vortex centers above the particle. Thereby, the distances between the two upper and the two lower vortex centers become more similar. The qualitative structure of the flow field thus changes differently for increasing σ than for increasing

L . Nevertheless, also for increasing σ from $\sigma = 0.5 \mu\text{m}$ to $\sigma = 5 \mu\text{m}$, we see that the flow near the particle becomes faster.

B. Strength of propulsion

Figure 3 shows our simulation results for the time-averaged stationary propulsion forces F_{\parallel} and F_{\perp} and torque T that act on the particle, their pressure components $F_{\parallel,p}$, $F_{\perp,p}$, and T_p , their viscous components $F_{\parallel,v}$, $F_{\perp,v}$, and T_v , and the corresponding translational propulsion velocities v_{\parallel} and v_{\perp} and angular propulsion velocity

ω of the particle.

1. Variation of length L

Again, we first consider a variation of the particle's length L while keeping the diameter σ constant.

To start, we focus on the parallel components of the propulsion (see Fig. 3a). When L increases, $F_{\parallel,p}$ decreases from $F_{\parallel,p} = -0.77$ fN to $F_{\parallel,p} = -1.92$ fN. On the other hand, $F_{\parallel,v}$ increases from $F_{\parallel,v} = 0.73$ fN to $F_{\parallel,v} = 1.25$ fN. Since $F_{\parallel,p}$ is dominant, the parallel propulsion force F_{\parallel} decreases from $F_{\parallel} = -0.044$ fN to $F_{\parallel} = -0.67$ fN. The parallel propulsion velocity v_{\parallel} has a similar trend. It decreases from $v_{\parallel} = -0.009 \mu\text{m s}^{-1}$ to $v_{\parallel} = -0.044 \mu\text{m s}^{-1}$. The finding that the particle speed $|v_{\parallel}|$ increases with L is in agreement with the observation of Section III A 1 that the flow near the particle becomes faster for increasing L . Since v_{\parallel} is always negative, the particle will move backward, i.e., towards its concave end. This finding is in line with available experimental results [20]. The same study, on the other hand, found a decrease in the particle speed for increasing L . This differs from our results but could be explained by the differences in their setup compared to our study. For example, their particle has a different diameter ($\sigma = 0.3 \mu\text{m}$) than our particle, they used a standing instead of a traveling ultrasound wave, and their ultrasound had a different frequency ($f = 3.77$ MHz).

Now, we consider the perpendicular components of the propulsion (see Fig. 3b). When L is increased, the force $F_{\perp,p}$ increases from $F_{\perp,p} = -0.0076$ fN to $F_{\perp,p} = 0.39$ fN. In contrast, $F_{\perp,v}$ only increases from $F_{\perp,v} = 0.061$ fN to $F_{\perp,v} = 0.098$ fN. The function for the perpendicular propulsion force F_{\perp} is therefore rather parallel to the curve for $F_{\perp,p}$ and increases from $F_{\perp} = 0.053$ fN to $F_{\perp} = 0.49$ fN. Since the translational hydrodynamic resistance of the particle also increases with L , the perpendicular propulsion velocity v_{\perp} is roughly constant at $v_{\perp} = 0.02 \mu\text{m s}^{-1}$.

Next, we address the rotational components of the propulsion (see Fig. 3c). For increasing L , the components T_p and T_v as well as the propulsion torque T are negative and further decreasing. T_p decreases from $T_p = -0.006$ fN μm to $T_p = -0.13$ fN μm , T_v decreases from $T_v = -0.045$ fN μm to $T_v = -0.094$ fN μm , and thus T decreases from $T = -0.051$ fN μm to $T = -0.23$ fN μm . The angular propulsion velocity ω , however, increases from $\omega = -0.12 \text{ s}^{-1}$ to zero, since the angular hydrodynamic resistance Ω_{33} of the particle increases steeply with L (see Tab. II). We can compare the, according to the amount, largest angular velocity $\omega = -0.12 \text{ s}^{-1}$ with the particle's rotation through Brownian motion. The latter is characterized by the particle's rotational diffusion coefficient $D_R = (k_B T_0 / \nu_s) (\mathbf{H}^{-1})_{66} = 8.47 \text{ s}^{-1}$, corresponding to rotation in the x_1 - x_2 plane, where k_B is the Boltzmann constant. Brownian rotation with this rotational diffusion coefficient is associated with a reorienta-

tion of the particle on the timescale 0.12 s . On the other hand, the angular velocity $\omega = -0.12 \text{ s}^{-1}$ corresponds to a reorientation by 90° in about 13 s . This shows that the Brownian rotation is dominant and the rotational acoustic propulsion can be ignored here, which is in line with the findings of previous studies that addressed other kinds of ultrasound-propelled particles [44, 49, 52–54].

For the limiting case of a hemi-spherical cup ($L = 0.1 \mu\text{m}$), we thus find that, according to the amount, the parallel propulsion velocity is particularly small, the perpendicular propulsion velocity is similar to that of longer bullet-shaped particles, and the angular propulsion is particularly large. We thus conclude that hemi-spherical cups are less suitable than longer bullet-shaped particles for transporting drugs or other cargo to a target, as it is a future scenario of nanomedicine [2, 7, 16, 18, 22, 23, 28, 30], since the former particles exhibit slower translational but faster rotational motion.

2. Variation of diameter σ

Again, we proceed to a variation of the particle's diameter σ while keeping the length L constant.

At first, we consider the parallel components of the propulsion (see Fig. 3d). When σ increases, $F_{\parallel,p}$ increases from $F_{\parallel,p} = -0.77$ fN to $F_{\parallel,p} = 332.67$ fN. On the contrary, $F_{\parallel,v}$ decreases from $F_{\parallel,v} = 0.73$ fN to $F_{\parallel,v} = -316.15$ fN. Since $F_{\parallel,p}$ is again dominant, the parallel propulsion force F_{\parallel} increases from $F_{\parallel} = -0.044$ fN to $F_{\parallel} = 16.52$ fN. The parallel propulsion velocity v_{\parallel} also increases, starting with $v_{\parallel} = -0.0085 \mu\text{m s}^{-1}$ and ending with $v_{\parallel} = 0.35 \mu\text{m s}^{-1}$. This overall increase of the particle speed with σ is in line with the observation of Section III A 2 that the flow near the particle becomes faster for increasing σ . While the particle moves backward – like the more elongated bullet-shaped particles that are considered in Section III B 1 – for diameter $\sigma = 0.5 \mu\text{m}$, it starts to move forward and rapidly increases its forward speed when σ is increased. This increase of v_{\parallel} is even steeper than the increase of v_{\parallel} with L (see Section III B 1). The sign change of the propulsion parallel to the particle orientation must occur somewhere between $\sigma = 0.5 \mu\text{m}$ and $\sigma = 1 \mu\text{m}$. These findings are consistent with the experimental results reported in Ref. [19], where a hemi-spherical-cup-shaped particle and a bullet-shaped particle were found to propel in opposite directions. The different signs of the propulsion were theoretically explained in Ref. [26]. Using an analytical approach, this study shows that such a sign change can occur at $\beta \in \mathcal{O}(1)$ with the acoustic Reynolds number $\beta = \pi \rho_0 \sigma^2 f / (2 \nu_s)$. The occurrence of the sign change between $\sigma = 0.5 \mu\text{m}$ and $\sigma = 1 \mu\text{m}$ in our simulations corresponds to a sign change between $\beta = 0.4$ and $\beta = 1.6$ in terms of the acoustic Reynolds number, which is consistent with the condition $\beta \in \mathcal{O}(1)$ presented in Ref. [26].

Now, we consider the perpendicular components of the

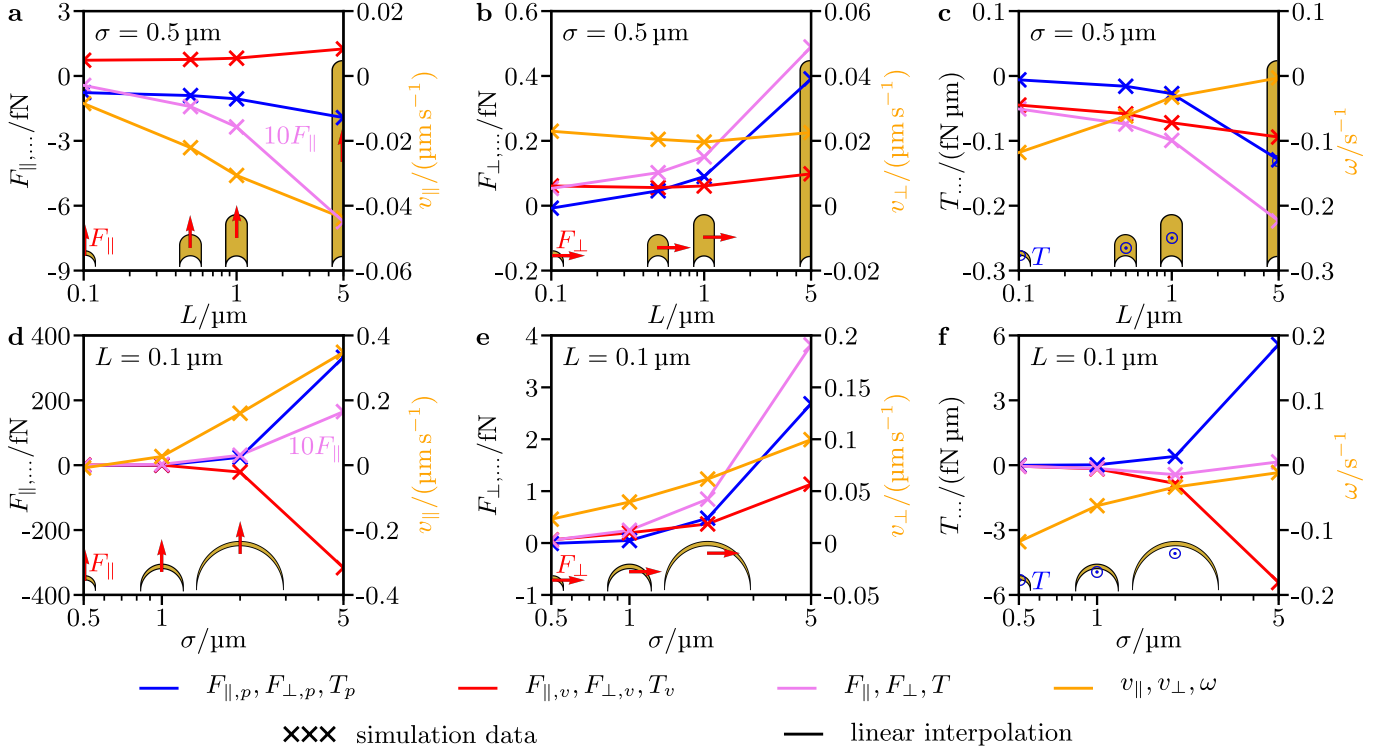


FIG. 3. Simulation data for the time averaged propulsion forces F_{\parallel} and F_{\perp} and torque T acting on the particle, their pressure components $F_{\parallel,p}$, $F_{\perp,p}$, and T_p , their viscous components $F_{\parallel,v}$, $F_{\perp,v}$, and T_v , and the corresponding translational propulsion velocities v_{\parallel} and v_{\perp} and angular propulsion velocity ω for various **a-c** particle lengths L with $\sigma = 0.5 \mu\text{m}$ and **d-f** particle diameters σ with $L = 0.1 \mu\text{m}$. In **a** and **d**, $10F_{\parallel}$ is shown instead of F_{\parallel} for better visibility of the course of the function.

propulsion (see Fig. 3e). When σ is increased, all perpendicular quantities $F_{\perp,p}$, $F_{\perp,v}$, F_{\perp} , and v_{\perp} grow. $F_{\perp,p}$ increases from $F_{\perp,p} = -0.0076 \text{ fN}$ to $F_{\perp,p} = 2.68 \text{ fN}$, $F_{\perp,v}$ increases from $F_{\perp,v} = 0.061 \text{ fN}$ to $F_{\perp,v} = 1.13 \text{ fN}$, the perpendicular propulsion force F_{\perp} increases from $F_{\perp} = 0.053 \text{ fN}$ to $F_{\perp} = 3.82 \text{ fN}$, and the perpendicular propulsion velocity v_{\perp} increases from $v_{\perp} = 0.023 \mu\text{m s}^{-1}$ to $v_{\perp} = 0.10 \mu\text{m s}^{-1}$.

Finally, we address the rotational components of the propulsion (see Fig. 3f). For increasing σ , the torque T_p increases from $T_p = -0.006 \text{ fN } \mu\text{m}$ to $T_p = 5.58 \text{ fN } \mu\text{m}$, whereas T_v decreases from $T_v = -0.045 \text{ fN } \mu\text{m}$ to $T_v = -5.43 \text{ fN } \mu\text{m}$. As a consequence, the propulsion torque T is rather constant and close to zero. However, the angular propulsion velocity ω strongly increases from $\omega = -0.12 \text{ s}^{-1}$ to $\omega = -0.011 \text{ s}^{-1}$, since the angular hydrodynamic resistance of the particle increases with σ . The, according to the amount, largest occurring angular propulsion velocity is here the same ($\omega = -0.12 \text{ s}^{-1}$) as in Fig. 3c and thus, as explained in Section III B 1, negligible compared to rotational Brownian motion.

IV. CONCLUSIONS

We have simulated a cylindrical particle with concave and convex hemi-spherical ends, as has been used in

many experiments [1–3, 6–9, 12, 13, 16, 18, 20, 22, 23, 27, 28, 30, 33–35, 38, 46, 48, 68, 69], in the presence of a planar traveling ultrasound wave. The particle has a variable cylinder length and diameter and includes (for a small cylinder length) hemi-spherical cups (nanoshells) [19, 37, 44] as a limiting case. On this basis, we have studied how the acoustic propulsion of such a bullet-shaped or cup-shaped particle depends on its length and diameter.

Our results show a strong dependence of the propulsion on the dimensions of the particle. For example, we found that the flow field around the particle is dominated by an assembly of vortices whose positions move in a complex way when the particle length or the particle diameter is varied. Furthermore, we found that translational propulsion of the particle parallel to its symmetry axis changes sign at small diameters and, according to the amount, increases with both the length and diameter of the particle. Especially a large diameter allows to reach large propulsion speeds. The angular propulsion of the particle, on the other hand, decreases when the length or diameter is increased. This suggests that larger particles exhibit a stronger and more translational motion than smaller particles.

These results are important since they contribute to a better understanding of the acoustic propulsion of nano- and microparticles, which will be a prerequisite for realizing the intriguing future applications that have been

envisaged for such particles [2, 7, 12, 13, 16, 18, 22, 23, 28, 30, 35, 38, 69, 76]. The obtained insights into how the acoustic propulsion depends on the shape parameters of the particles will prospectively prove useful for selecting suitable particle designs for coming experimental studies. Although we have studied here two very common types of ultrasound-propelled particles, further studies that focus on other particle shapes will be required to complement the understanding of how acoustic propulsion depends on the particle shape.

DATA AVAILABILITY

The data that support the findings of this study are openly available in <https://doi.org/10.5281/zenodo.5913332>.

5913332.

CONFLICTS OF INTEREST

There are no conflicts of interest to declare.

ACKNOWLEDGMENTS

We thank Patrick Kurzeja for helpful discussions. R.W. is funded by the Deutsche Forschungsgemeinschaft (DFG, German Research Foundation) – WI 4170/3-1. The simulations for this work were performed on the computer cluster PALMA II of the University of Münster.

- [1] W. Wang, L. Castro, M. Hoyos, and T. E. Mallouk, “Autonomous motion of metallic microrods propelled by ultrasound,” *ACS Nano* **6**, 6122–6132 (2012).
- [2] V. Garcia-Gradilla, J. Orozco, S. Sattayasamitsathit, F. Soto, F. Kuralay, A. Pourazary, A. Katzenberg, W. Gao, Y. Shen, and J. Wang, “Functionalized ultrasound-propelled magnetically guided nanomotors: toward practical biomedical applications,” *ACS Nano* **7**, 9232–9240 (2013).
- [3] S. Ahmed, W. Wang, L. O. Mair, R. D. Fraleigh, S. Li, L. A. Castro, M. Hoyos, T. J. Huang, and T. E. Mallouk, “Steering acoustically propelled nanowire motors toward cells in a biologically compatible environment using magnetic fields,” *Langmuir* **29**, 16113–16118 (2013).
- [4] F. Nadal and E. Lauga, “Asymmetric steady streaming as a mechanism for acoustic propulsion of rigid bodies,” *Physics of Fluids* **26**, 082001 (2014).
- [5] Z. Wu, T. Li, J. Li, W. Gao, T. Xu, C. Christianson, W. Gao, M. Galarnyk, Q. He, L. Zhang, *et al.*, “Turning erythrocytes into functional micromotors,” *ACS Nano* **8**, 12041–12048 (2014).
- [6] W. Wang, S. Li, L. Mair, S. Ahmed, T. J. Huang, and T. E. Mallouk, “Acoustic propulsion of nanorod motors inside living cells,” *Angewandte Chemie International Edition* **53**, 3201–3204 (2014).
- [7] V. Garcia-Gradilla, S. Sattayasamitsathit, F. Soto, F. Kuralay, C. Yardımcı, D. Wiitala, M. Galarnyk, and J. Wang, “Ultrasound-propelled nanoporous gold wire for efficient drug loading and release,” *Small* **10**, 4154–4159 (2014).
- [8] A. L. Balk, L. O. Mair, P. P. Mathai, P. N. Patrone, W. Wang, S. Ahmed, T. E. Mallouk, J. A. Liddle, and S. M. Stavis, “Kilohertz rotation of nanorods propelled by ultrasound, traced by microvortex advection of nanoparticles,” *ACS Nano* **8**, 8300–8309 (2014).
- [9] S. Ahmed, D. T. Gentekos, C. A. Fink, and T. E. Mallouk, “Self-assembly of nanorod motors into geometrically regular multimers and their propulsion by ultrasound,” *ACS Nano* **8**, 11053–11060 (2014).
- [10] D. Ahmed, M. Lu, A. Nourhani, P. E. Lammert, Z. Stratton, H. S. Muddana, V. H. Crespi, and T. J. Huang, “Selectively manipulable acoustic-powered microswimmers,” *Scientific Reports* **5**, 9744 (2015).
- [11] W. Wang, W. Duan, Z. Zhang, M. Sun, A. Sen, and T. E. Mallouk, “A tale of two forces: simultaneous chemical and acoustic propulsion of bimetallic micromotors,” *Chemical Communications* **51**, 1020–1023 (2015).
- [12] B. Esteban-Fernández de Ávila, A. Martín, F. Soto, M. A. Lopez-Ramirez, S. Campuzano, G. M. Vásquez-Machado, W. Gao, L. Zhang, and J. Wang, “Single cell real-time miRNAs sensing based on nanomotors,” *ACS Nano* **9**, 6756–6764 (2015).
- [13] Z. Wu, T. Li, W. Gao, W. Xu, B. Jurado-Sánchez, J. Li, W. Gao, Q. He, L. Zhang, and J. Wang, “Cell-membrane-coated synthetic nanomotors for effective biodegradation,” *Advanced Functional Materials* **25**, 3881–3887 (2015).
- [14] Z. Wu, B. Esteban-Fernández de Ávila, A. Martín, C. Christianson, W. Gao, S. K. Thamphiwatana, A. Escarpa, Q. He, L. Zhang, and J. Wang, “RBC micromotors carrying multiple cargos towards potential theranostic applications,” *Nanoscale* **7**, 13680–13686 (2015).
- [15] K. J. Rao, F. Li, L. Meng, H. Zheng, F. Cai, and W. Wang, “A force to be reckoned with: a review of synthetic microswimmers powered by ultrasound,” *Small* **11**, 2836–2846 (2015).
- [16] M. Kiristi, V. Singh, B. Esteban-Fernández de Ávila, M. Uygun, F. Soto, D. Aktas Uygun, and J. Wang, “Lysozyme-based antibacterial nanomotors,” *ACS Nano* **9**, 9252–9259 (2015).
- [17] K. Kim, J. Guo, Z. Liang, F. Zhu, and D. Fan, “Man-made rotary nanomotors: a review of recent developments,” *Nanoscale* **8**, 10471–10490 (2016).
- [18] B. Esteban-Fernández de Ávila, C. Angell, F. Soto, M. A. Lopez-Ramirez, D. F. Báez, S. Xie, J. Wang, and Y. Chen, “Acoustically propelled nanomotors for intracellular siRNA delivery,” *ACS Nano* **10**, 4997–5005 (2016).
- [19] F. Soto, G. L. Wagner, V. Garcia-Gradilla, K. T. Gillespie, D. R. Lakshminpathy, E. Karshalev, C. Angell, Y. Chen, and J. Wang, “Acoustically propelled nanoshells,” *Nanoscale* **8**, 17788–17793 (2016).

- [20] S. Ahmed, W. Wang, L. Bai, D. T. Gentekos, M. Hoyos, and T. E. Mallouk, "Density and shape effects in the acoustic propulsion of bimetallic nanorod motors," *ACS Nano* **10**, 4763–4769 (2016).
- [21] M. Kaynak, A. Ozcelik, N. Nama, A. Nourhani, P. E. Lammert, V. H. Crespi, and T. J. Huang, "Acoustofluidic actuation of in situ fabricated microrotors," *Lab on a Chip* **16**, 3532–3537 (2016).
- [22] M. Uygun, B. Jurado-Sánchez, D. A. Uygun, V. V. Singh, L. Zhang, and J. Wang, "Ultrasound-propelled nanowire motors enhance asparaginase enzymatic activity against cancer cells," *Nanoscale* **9**, 18423–18429 (2017).
- [23] B. Esteban-Fernández de Ávila, D. E. Ramírez-Herrera, S. Campuzano, P. Angsantikul, L. Zhang, and J. Wang, "Nanomotor-enabled pH-responsive intracellular delivery of caspase-3: toward rapid cell apoptosis," *ACS Nano* **11**, 5367–5374 (2017).
- [24] L. Ren, D. Zhou, Z. Mao, P. Xu, T. J. Huang, and T. E. Mallouk, "Rheotaxis of bimetallic micromotors driven by chemical-acoustic hybrid power," *ACS Nano* **11**, 10591–10598 (2017).
- [25] M. Kaynak, A. Ozcelik, A. Nourhani, P. E. Lammert, V. H. Crespi, and T. J. Huang, "Acoustic actuation of bioinspired microswimmers," *Lab on a Chip* **17**, 395–400 (2017).
- [26] J. F. Collis, D. Chakraborty, and J. E. Sader, "Autonomous propulsion of nanorods trapped in an acoustic field," *Journal of Fluid Mechanics* **825**, 29–48 (2017).
- [27] C. Zhou, L. Zhao, M. Wei, and W. Wang, "Twists and turns of orbiting and spinning metallic microparticles powered by megahertz ultrasound," *ACS Nano* **11**, 12668–12676 (2017).
- [28] C. Zhou, J. Yin, C. Wu, L. Du, and Y. Wang, "Efficient target capture and transport by fuel-free micromotors in a multichannel microchip," *Soft Matter* **13**, 8064–8069 (2017).
- [29] X.-Z. Chen, B. Jang, D. Ahmed, C. Hu, C. De Marco, M. Hoop, F. Mushtaq, B. J. Nelson, and S. Pané, "Small-scale machines driven by external power sources," *Advanced Materials* **30**, 1705061 (2018).
- [30] M. Hansen-Bruhn, B. Esteban-Fernández de Ávila, M. Beltrán-Gastélum, J. Zhao, D. E. Ramírez-Herrera, P. Angsantikul, K. Vesterager Gothelf, L. Zhang, and J. Wang, "Active intracellular delivery of a Cas9/sgRNA complex using ultrasound-propelled nanomotors," *Angewandte Chemie International Edition* **57**, 2657–2661 (2018).
- [31] S. Sabrina, M. Tasinkevych, S. Ahmed, A. M. Brooks, M. Olvera de la Cruz, T. E. Mallouk, and K. J. M. Bishop, "Shape-directed microspinners powered by ultrasound," *ACS Nano* **12**, 2939–2947 (2018).
- [32] D. Ahmed, T. Baasch, B. Jang, S. Pane, J. Dual, and B. J. Nelson, "Artificial swimmers propelled by acoustically activated flagella," *Nano Letters* **16**, 4968–4974 (2016).
- [33] D. Zhou, Y. Gao, J. Yang, Y. C. Li, G. Shao, G. Zhang, T. Li, and L. Li, "Light-ultrasound driven collective "firework" behavior of nanomotors," *Advanced Science* **5**, 1800122 (2018).
- [34] D. Wang, C. Gao, W. Wang, M. Sun, B. Guo, H. Xie, and Q. He, "Shape-transformable, fusible rodlike swimming liquid metal nanomachine," *ACS Nano* **12**, 10212–10220 (2018).
- [35] B. Esteban-Fernández de Ávila, P. Angsantikul, D. E. Ramírez-Herrera, F. Soto, H. Teymourian, D. Dehaini, Y. Chen, L. Zhang, and J. Wang, "Hybrid biomembrane-functionalized nanorobots for concurrent removal of pathogenic bacteria and toxins," *Science Robotics* **3**, eaat0485 (2018).
- [36] X. Lu, H. Shen, Z. Wang, K. Zhao, H. Peng, and W. Liu, "Micro/Nano machines driven by ultrasound power sources," *Chemistry – An Asian Journal* **14**, 2406–2416 (2019).
- [37] S. Tang, F. Zhang, J. Zhao, W. Talaat, F. Soto, E. Karshalev, C. Chen, Z. Hu, X. Lu, J. Li, *et al.*, "Structure-dependent optical modulation of propulsion and collective behavior of acoustic/light-driven hybrid microbowls," *Advanced Functional Materials* **29**, 1809003 (2019).
- [38] J. R. Qualliotine, G. Bolat, M. Beltrán-Gastélum, B. Esteban-Fernández de Ávila, J. Wang, and J. A. Califano, "Acoustic nanomotors for detection of human papillomavirus-associated head and neck cancer," *Otolaryngology–Head and Neck Surgery* **161**, 814–822 (2019).
- [39] C. Gao, Z. Lin, D. Wang, Z. Wu, H. Xie, and Q. He, "Red blood cell-mimicking micromotor for active photodynamic cancer therapy," *ACS Applied Materials & Interfaces* **11**, 23392–23400 (2019).
- [40] L. Ren, N. Nama, J. M. McNeill, F. Soto, Z. Yan, W. Liu, W. Wang, J. Wang, and T. E. Mallouk, "3D steerable, acoustically powered microswimmers for single-particle manipulation," *Science Advances* **5**, eaax3084 (2019).
- [41] T. Bhuyan, D. Dutta, M. Bhattacharjee, A. Singh, S. Ghosh, and D. Bandyopadhyay, "Acoustic propulsion of vitamin C loaded teabots for targeted oxidative stress and amyloid therapeutics," *ACS Applied Bio Materials* **2**, 4571–4582 (2019).
- [42] A. Aghakhani, O. Yasa, P. Wrede, and M. Sitti, "Acoustically powered surface-slipping mobile microrobots," *Proceedings of the National Academy of Sciences U.S.A.* **117**, 3469–3477 (2020).
- [43] J. Liu and H. Ruan, "Modeling of an acoustically actuated artificial micro-swimmer," *Bioinspiration & Biomimetics* **15**, 036002 (2020).
- [44] J. Voß and R. Wittkowski, "On the shape-dependent propulsion of nano- and microparticles by traveling ultrasound waves," *Nanoscale Advances* **2**, 3890–3899 (2020).
- [45] M. Valdez-Garduño, M. Leal-Estrada, E. S. Oliveros-Mata, D. I. Sandoval-Bojorquez, F. Soto, J. Wang, and V. Garcia-Gradilla, "Density asymmetry driven propulsion of ultrasound-powered Janus micromotors," *Advanced Functional Materials* **30**, 2004043 (2020).
- [46] G. Dumy, N. Jeger-Madiot, X. Benoit-Gonin, T. Mallouk, M. Hoyos, and J. Aider, "Acoustic manipulation of dense nanorods in microgravity," *Microgravity Science and Technology* **32**, 1159–1174 (2020).
- [47] J. McNeill, N. Nama, J. Braxton, and T. Mallouk, "Wafer-scale fabrication of micro- to nanoscale bubble swimmers and their fast autonomous propulsion by ultrasound," *ACS Nano* **14**, 7520–7528 (2020).
- [48] J. McNeill, N. Sinai, J. Wang, V. Oliver, E. Lauga, F. Nadal, and T. Mallouk, "Purely viscous acoustic propulsion of bimetallic rods," *Physical Review Fluids* **6**, L092201 (2021).

- [49] J. Voß and R. Wittkowski, “Acoustically propelled nano- and microcones: fast forward and backward motion,” *Nanoscale Advances* **4**, 281–293 (2022).
- [50] S. Mohanty, J. Zhang, J. McNeill, T. Kuenen, F. Linde, J. Rouwkema, and S. Misra, “Acoustically-actuated bubble-powered rotational micro-propellers,” *Sensors and Actuators B: Chemical* **347**, 130589 (2021).
- [51] J. Li, C. Mayorga-Martinez, C. Ohl, and M. Pumera, “Ultrasonically propelled micro- and nanorobots,” *Advanced Functional Materials* **32**, 2102265 (2022).
- [52] J. Voß and R. Wittkowski, “Orientation-dependent propulsion of triangular nano- and microparticles by a traveling ultrasound wave,” *ACS Nano*, provisionally accepted (2022).
- [53] J. Voß and R. Wittkowski, “Acoustic propulsion of nano- and microcones: dependence on particle size, acoustic energy density, and sound frequency,” submitted (2022).
- [54] J. Voß and R. Wittkowski, “Acoustic propulsion of nano- and microcones: dependence on the viscosity of the surrounding fluid,” submitted (2022).
- [55] J. Voß and R. Wittkowski, “Ultrasound-propelled nano- and microspinnners,” submitted (2022).
- [56] J. Li, B. Esteban-Fernández de Ávila, W. Gao, L. Zhang, and J. Wang, “Micro/Nanorobots for biomedicine: delivery, surgery, sensing, and detoxification,” *Science Robotics* **2**, eaam6431 (2017).
- [57] F. Peng, Y. Tu, and D. A. Wilson, “Micro/Nanomotors towards in vivo application: cell, tissue and biofluid,” *Chemical Society Reviews* **46**, 5289–5310 (2017).
- [58] F. Soto and R. Chrostowski, “Frontiers of medical micro/nanorobotics: in vivo applications and commercialization perspectives toward clinical uses,” *Frontiers in Bioengineering and Biotechnology* **6**, 170 (2018).
- [59] D. Wang, C. Gao, C. Zhou, Z. Lin, and Q. He, “Leukocyte membrane-coated liquid metal nanoswimmers for actively targeted delivery and synergistic chemophotothermal therapy,” *Research* **2020**, 3676954 (2020).
- [60] W. Wang and C. Zhou, “A journey of nanomotors for targeted cancer therapy: Principles, challenges, and a critical review of the state-of-the-art,” *Advanced Healthcare Materials* **10**, 2001236 (2021).
- [61] M. Leal-Estrada, M. Valdez-Garduño, F. Soto, and V. Garcia-Gradilla, “Engineering ultrasound fields to power medical micro/nanorobots,” *Current Robotics Reports* **2**, 21–32 (2021).
- [62] T. Nitschke and R. Wittkowski, “Collective guiding of acoustically propelled nano- and microparticles for medical applications,” *arXiv:2112.13676* (2021).
- [63] I. Jun and H. Hess, “A biomimetic, self-pumping membrane,” *Advanced Materials* **22**, 4823–4825 (2010).
- [64] J. McDermott, A. Kar, M. Daher, S. Klara, G. Wang, A. Sen, and D. Velegol, “Self-generated diffusioosmotic flows from calcium carbonate micropumps,” *Langmuir* **28**, 15491–15497 (2012).
- [65] P. Fratzl, M. Friedman, K. Krauthausen, and W. Schäffner, eds., *Active Materials*, 1st ed. (De Gruyter, Berlin, 2021).
- [66] J. Li, T. Li, T. Xu, M. Kiristi, W. Liu, Z. Wu, and J. Wang, “Magneto-acoustic hybrid nanomotor,” *Nano Letters* **15**, 4814–4821 (2015).
- [67] L. Ren, W. Wang, and T. E. Mallouk, “Two forces are better than one: combining chemical and acoustic propulsion for enhanced micromotor functionality,” *Accounts of Chemical Research* **51**, 1948–1956 (2018).
- [68] T. Xu, F. Soto, W. Gao, R. Dong, V. Garcia-Gradilla, E. Magana, X. Zhang, and J. Wang, “Reversible swarming and separation of self-propelled chemically powered nanomotors under acoustic fields,” *Journal of the American Chemical Society* **137**, 2163–2166 (2015).
- [69] M. Beltrán-Gastélum, B. Esteban-Fernández de Ávila, H. Gong, P. L. Venugopalan, T. Hianik, J. Wang, and V. Subjakova, “Rapid detection of AIB1 in breast cancer cells based on aptamer-functionalized nanomotors,” *ChemPhysChem* **20**, 3177–3180 (2019).
- [70] S. B. Barnett, G. R. ter Haar, M. C. Ziskin, H. D. Rott, F. A. Duck, and K. Maeda, “International recommendations and guidelines for the safe use of diagnostic ultrasound in medicine,” *Ultrasound in Medicine & Biology* **26**, 355–366 (2000).
- [71] M. J. Holmes, N. G. Parker, and M. J. W. Povey, “Temperature dependence of bulk viscosity in water using acoustic spectroscopy,” *Journal of Physics: Conference Series* **269**, 012011 (2011).
- [72] H. G. Weller, G. Tabor, H. Jasak, and C. Fureby, “A tensorial approach to computational continuum mechanics using object-oriented techniques,” *Computers in Physics* **12**, 620–631 (1998).
- [73] J. Happel and H. Brenner, *Low Reynolds Number Hydrodynamics: With Special Applications to Particulate Media*, 2nd ed., *Mechanics of Fluids and Transport Processes*, Vol. 1 (Kluwer Academic Publishers, Dordrecht, 1991).
- [74] J. Voß and R. Wittkowski, “Hydrodynamic resistance matrices of colloidal particles with various shapes,” *arXiv:1811.01269* (2018).
- [75] J. Voß, J. Jeggle, and R. Wittkowski, “HydResMat – FEM-based code for calculating the hydrodynamic resistance matrix of an arbitrarily-shaped colloidal particle,” *Zenodo* (2019), DOI: 10.5281/zenodo.3541588.
- [76] P. Venugopalan, B. Esteban-Fernández de Ávila, M. Pal, A. Ghosh, and J. Wang, “Fantastic voyage of nanomotors into the cell,” *ACS Nano* **14**, 9423–9439 (2020).